

Observation in the MINOS far detector of the shadowing of cosmic rays by the sun and moon

P. Adamson^g C. Andreopoulos^{x,b} D. S. Ayres^a C. Backhouse^t
 G. Barr^t W. L. Barrett^{ag} M. Bishai^d A. Blake^f B. Bock^r
 G. J. Bock^g D. J. Boehnlein^g D. Bogert^g C. Bower^m S. Budd^a
 S. Cavanaughⁱ D. Cherdack^{ac} S. Childress^g B. C. Choudhary^{g,e,2}
 J. H. Cobb^t J. A. B. Coelho^{ad} S. J. Coleman^{ah} L. Corwin^m
 D. Cronin-Hennessy^q I. Z. Danko^u J. K. de Jong^{t,k}
 N. E. Devenish^z M. V. Diwan^d M. Dorman^p C. O. Escobar^{ad}
 J. J. Evans^p E. Falk^z G. J. Feldmanⁱ M. V. Frohne^{j,c}
 H. R. Gallagher^{ac} A. Godley^w R. Gomes^h M. C. Goodman^a
 P. Gouffon^{ae} R. Gran^r N. Grant^x E. W. Grashorn^{q,r,*,4}
 K. Grzelak^{af,t} A. Habig^r D. Harris^g P. G. Harris^z J. Hartnell^{z,x}
 R. Hatcher^g A. Himmel^e A. Holin^p X. Huang^a J. Hylan^g J. Ilic^x
 G. M. Irwin^y Z. Isvan^u D. E. Jaffe^d C. James^g D. Jensen^g
 T. Kafka^{ac} S. M. S. Kasahara^q G. Koizumi^g S. Kopp^{ab}
 M. Kordosky^{ah,p} Z. Krahn^q A. Kreymer^g K. Lang^{ab} G. Lefeuvre^z
 J. Ling^w P. J. Litchfield^q R. P. Litchfield^t L. Loiacono^{ab} P. Lucas^g
 J. Ratchford^{ab} W. A. Mann^{ac} M. L. Marshak^q J. S. Marshall^f
 N. Mayer^m A. M. McGowan^{a,q,5} R. Mehdiev^{ab} J. R. Meier^q
 M. D. Messier^m D. G. Michael^{e,6} W. H. Miller^q S. R. Mishra^w
 J. Mitchell^f C. D. Moore^g L. Mualem^e S. Mufson^m J. Musser^m
 D. Naples^u J. K. Nelson^{ah} H. B. Newman^e R. J. Nichol^p
 T. C. Nicholls^x W. P. Oliver^{ac} M. Orchanian^e J. Paley^{a,m}
 R. B. Patterson^e G. Pawloski^y G. F. Pearce^x E. A. Peterson^q
 R. Pittam^t R. K. Plunkett^g T. M. Raufer^{x,t} B. Rebel^g
 J. Reichenbacher^{a,1} P. A. Rodrigues^t C. Rosenfeld^w H. A. Rubin^k
 V. A. Ryabovⁿ M. C. Sanchez^{l,a,i} J. Schneps^{ac} P. Schreiner^c
 V. K. Semenov^v P. Shanahan^g A. Sousa^{i,t} M. Strait^q N. Tagg^{s,ac}
 R. L. Talaga^a J. Thomas^p M. A. Thomson^f J. L. Thron^{a,3} G. Tinti^t
 R. Toner^f G. Tzanakos^b J. Urheim^m P. Vahle^{ah,p} B. Viren^d
 A. Weber^t R. C. Webb^{aa} C. White^k L. Whitehead^d S. G. Wojcicki^y

D. M. Wright^o T. Yang^y R. Zwaska^g

^a*Argonne National Laboratory, Argonne, Illinois 60439, USA*

^b*Department of Physics, University of Athens, GR-15771 Athens, Greece*

^c*Physics Department, Benedictine University, Lisle, Illinois 60532, USA*

^d*Brookhaven National Laboratory, Upton, New York 11973, USA*

^e*Lauritsen Laboratory, California Institute of Technology, Pasadena, California 91125, USA*

^f*Cavendish Laboratory, University of Cambridge, Madingley Road, Cambridge CB3 0HE, United Kingdom*

^g*Fermi National Accelerator Laboratory, Batavia, Illinois 60510, USA*

^h*Universidade Federal de Goias, Instituto de Fisica, CP 131, 74001-970, Goiania, Goias, Brazil*

ⁱ*Department of Physics, Harvard University, Cambridge, Massachusetts 02138, USA*

^j*Holy Cross College, Notre Dame, Indiana 46556, USA*

^k*Physics Division, Illinois Institute of Technology, Chicago, Illinois 60616, USA*

^l*Department of Physics and Astronomy, Iowa State University, Ames, Iowa 50011, USA*

^m*Indiana University, Bloomington, Indiana 47405, USA*

ⁿ*Nuclear Physics Department, Lebedev Physical Institute, Leninsky Prospect 53, 119991 Moscow, Russia*

^o*Lawrence Livermore National Laboratory, Livermore, California 94550, USA*

^p*Department of Physics and Astronomy, University College London, Gower Street, London WC1E 6BT, United Kingdom*

^q*University of Minnesota, Minneapolis, Minnesota 55455, USA*

^r*Department of Physics, University of Minnesota – Duluth, Duluth, Minnesota 55812, USA*

^s*Otterbein College, Westerville, Ohio 43081, USA*

^t*Subdepartment of Particle Physics, University of Oxford, Oxford OX1 3RH, United Kingdom*

^u*Department of Physics and Astronomy, University of Pittsburgh, Pittsburgh, Pennsylvania 15260, USA*

^v*Institute for High Energy Physics, Protvino, Moscow Region RU-140284, Russia*

^w*Department of Physics and Astronomy, University of South Carolina, Columbia, South Carolina 29208, USA*

^x*Rutherford Appleton Laboratory, Science and Technology Facilities Council, OX11 0QX, United Kingdom*

^y*Department of Physics, Stanford University, Stanford, California 94305, USA*

^z*Department of Physics and Astronomy, University of Sussex, Falmer, Brighton BN1 9QH, United Kingdom*

^{aa}*Physics Department, Texas A&M University, College Station, Texas 77843, USA*

^{ab}*Department of Physics, University of Texas at Austin, 1 University Station C1600,
Austin, Texas 78712, USA*

^{ac}*Physics Department, Tufts University, Medford, Massachusetts 02155, USA*

^{ad}*Universidade Estadual de Campinas, IFGW-UNICAMP, CP 6165, 13083-970,
Campinas, SP, Brazil*

^{ae}*Instituto de Física, Universidade de São Paulo, CP 66318, 05315-970, São Paulo, SP,
Brazil*

^{af}*Department of Physics, University of Warsaw, Hoża 69, PL-00-681 Warsaw, Poland*

^{ag}*Physics Department, Western Washington University, Bellingham, Washington 98225,
USA*

^{ah}*Department of Physics, College of William & Mary, Williamsburg, Virginia 23187, USA*

Abstract

The shadowing of cosmic ray primaries by the the moon and sun was observed by the MINOS far detector at a depth of 2070 mwe using 83.54 million cosmic ray muons accumulated over 1857.91 live-days. The shadow of the moon was detected at the 5.6σ level and the shadow of the sun at the 3.8σ level using a log-likelihood search in celestial coordinates. The moon shadow was used to quantify the absolute astrophysical pointing of the detector to be $0.17\pm 0.12^\circ$. Hints of Interplanetary Magnetic Field effects were observed in both the sun and moon shadow.

1 Introduction & Motivation

The Main Injector Neutrino Oscillation Search (MINOS) far detector [1] is a magnetized scintillator and steel tracking calorimeter, located in the Soudan Mine, ($47^\circ 49' 13.3''$ N, $92^\circ 14' 28.5''$ W) in northern Minnesota, USA, at a depth of 2070 meters water equivalent (mwe). While the primary function of the far detector is to detect neutrinos from Fermilab's NuMI ν_μ beam [2], the

* Corresponding author.

Email address: grashorn@mps.ohio-state.edu (E. W. Grashorn).

¹ Now at Department of Physics and Astronomy, University of Alabama, Tuscaloosa, Alabama 35487, USA.

² Now at Department of Physics and Astrophysics, University of Delhi, Delhi 110007, India.

³ Now at Nuclear Nonproliferation Division, Threat Reduction Directorate, Los Alamos National Laboratory, Los Alamos, New Mexico 87545, USA.

⁴ Now at Department of Physics, Ohio State University, Columbus, Ohio 42310, USA.

⁵ Now at Physics Department, St. John Fisher College, Rochester, New York 14618 USA.

⁶ Deceased.

great depth and wide acceptance of the detector combined with the flat overburden of the Soudan site allow it to serve as an efficient cosmic-ray muon detector. The 5.4 kton detector is composed of 486 8 m wide octagonal planes, each consisting of a 2.54 cm thick steel plate and a 1.0 cm thick scintillator plane. Adjacent planes are separated by a 2.4 cm air gap. It is 30 m long and has a total aperture of $6.91 \times 10^6 \text{ cm}^2 \text{ sr}$ [3] for the cosmic rays selected in this analysis. MINOS observes underground muons with a minimum surface energy of 0.7 TeV, and the sharply peaked energy spectrum has a mean value of about 1.0 TeV [4]. This mean muon energy corresponds to a mean cosmic ray primary energy of about 10 TeV.

Optical telescopes use a standard catalog of stars to establish the resolution and pointing reliability of a new instrument. This is not possible for a cosmic ray detector as there are no known cosmic ray sources available for calibration [5]. The shadow caused by the absorption of cosmic rays by the moon is a well observed phenomenon in the otherwise isotropic cosmic ray sky [6]. This shadow provides a means of studying the resolution and alignment of the detector which are important in the search for cosmic point sources. The physical extent and shape of the shadow gives information about the resolution of the detector, while the location of the deficit center measures the absolute pointing of the detector. The moon has a 0.52° diameter as viewed from earth, and the cosmic ray deficit it causes has been measured by air shower arrays (CYGNUS [7], CASA [8], Tibet [9], Milagro [10], GRAPES [11], HEGRA [12]) as well as underground detectors (Soudan 2 [13], MACRO [14,15], L3+C [16], BUST [17]).

The shadow of the moon is affected by multiple Coulomb scattering, the geomagnetic field and the Interplanetary Magnetic Field (IMF) [13]. Multiple Coulomb scattering occurs in the rock overburden and causes a general spreading of the moon deficit disc. The geomagnetic field is nearly a dipole and causes an eastward deflection of positive primaries, which results in a positive horizontal shift in the observed shadow of up to $\Delta\alpha = 0.15^\circ Z/E_p(\text{TeV})$ (see Sec. 2.2). Older calculations using an impulse approximation give a larger value [18,19]. The IMF is produced by the sun, which has an ambient dipole field that is 100 times greater than the geomagnetic field. The field is carried through the solar system by the solar wind, the stream of energetic charged particles that emanate from the atmosphere of the sun. Since the sun has a 27 day rotation period, the magnetic field has a spiral shape, called a Parker spiral [20]. The IMF causes a deflection of primaries that strongly depends on the solar wind. It changes in time and has a sectorized structure [21]. This complex structure makes it hard to model. The direction of the IMF vector is either “towards” or “away” from the earth and the two field directions are separated by a thin, field-free, region known as the “neutral current sheet”. The IMF causes a deflection that smears the moon’s shadow, though this effect is small since a cosmic ray primary travels a relatively short distance from the moon to earth. The larger IMF effect comes from its distortion of the geomagnetic field.

The sun also subtends a disk of diameter 0.52° , and in principle produces a similar shadow to the moon. Its shadow has been observed by CYGNUS [7], Tibet [9,22] and MACRO [15]. However, the much greater distance that cosmic primaries travel in the IMF can produce significant distortions in the shadow. The IMF varies according to the 11 year solar activity cycle and peaks at solar maximum, when the sun’s magnetic field changes polarity [23]. The most recent solar maximum occurred in February, 2001, and the following minimum occurred in December, 2008. The average magnitude of the IMF over the period of time that the MINOS data were collected was 6.5 nT. The

maximum value was 50 nT. Assuming a constant, uniform field and a 10 TeV proton, the average magnetic deflection is about 0.05° . For a 10 TeV proton traveling along the line from the Sun to the earth, the deflection is up to 0.75° . Because of the complex structure of the IMF already mentioned, the assumption of a constant, uniform field is not correct. By measuring the behavior of an ensemble of particles, thus sampling many parts of the IMF, a more refined understanding of the average IMF properties can be obtained.

1.1 Spherical Coordinate Systems

Horizon coordinates use the detector's local horizon as the fundamental plane. The longitudinal angle is azimuth (Az), measured east from north and ranges from 0° to 360° . The angle out of the equatorial plane is zenith (Zen), where vertical up has a value of 0° and the horizon has a value of 90° . Zenith is measured from 0° to 180° . Celestial coordinates are projected on the sky and centered on the earth's equatorial plane. The longitudinal angle is right ascension (RA), measured eastward from the Vernal equinox and ranges from 0° to 360° . The angle out of the equatorial plane is declination (Dec), ranging between $\pm 90^\circ$. Ecliptic coordinates are celestial coordinates that use the ecliptic (the path the sun follows over the course of a year) as its fundamental plane. The longitudinal angle is ecliptic longitude (λ), and is the same as RA . The angle out of the plane of the ecliptic is ecliptic latitude (β), ranging between $\pm 90^\circ$.

2 Data

In order to perform the shadowing analysis, the muon data must be selected for reliable pointing, the smearing and systematic offsets of the shadow must be understood, and the backgrounds must be quantified.

2.1 Event Selection

This analysis encompassed events recorded over 1980 days, from August 1, 2003 to December 31, 2008, giving a total of 1857.91 live-days when the detector was operational. The data set includes 83.54 million cosmic ray induced muon tracks. Cosmic ray muons were triggered by recording hits on four planes within a group of five planes. Several selection criteria were required to ensure that the detector was in a reliable state when the data were taken (Pre-Analysis selection criteria) and that only well reconstructed tracks were included in the sample (Analysis selection criteria). The Pre-Analysis selection criteria are described in [24]. The following analysis selection criteria were applied:

- (1) "Number of Planes > 9 ", a track that passes fewer planes may not give reliable localization information to the track fitter.

- (2) “Track Length > 1.55 m”, any event with a track shorter than 1.55 m may not be reliably reconstructed.
- (3) “ $|\vec{\sigma}_{vtx} - \vec{\sigma}_{end}| < 0.021$ m” If the uncertainty on the endpoint position, $\vec{\sigma}_{end}$, is significantly different from the uncertainty on the beginning position, $\vec{\sigma}_{vtx}$, then the muon has questionable reconstruction pointing. $|\vec{\sigma}_{vtx} - \vec{\sigma}_{end}|$ is a measure of the absolute value of the difference in track beginning and endpoint uncertainty.

These selection criteria were chosen to optimize the selection of cosmic ray muons with good pointing resolution on the sky. The cut values were determined empirically using standard MINOS *Monte Carlo* events, inserting the moon, and maximizing the moon shadow. The number of muons that survived each cut is shown in Table 1. Of the initial 83.54 million triggers, 62.5% survived all cuts, leaving 52.19 million muons.

Table 1

Fraction of events that survive each pointing cut

Cut	No. Remaining	Fraction Remaining
Total Tracks	83.54×10^6	1.0
1. Data Quality Cuts [24]	68.91×10^6	0.825
2. Number of Planes < 10	62.06×10^6	0.743
3. Track Length < 1.55 m	60.10×10^6	0.730
4. $ \vec{\sigma}_{vtx} - \vec{\sigma}_{end} > 0.021$	52.19×10^6	0.625

There are 17,389 muons in a 2° half-angle cone centered on the moon and 16,411 muons in a 2° half-angle cone centered on the sun. The reason for this difference is that the detector is at a high latitude, thus the number of muons collected in winter near the sun’s location will be fewer than the number collected near the moon. The data set includes five full yearly cycles plus five months. Those extra months came after the summer solstice, so the amount of time the sun spends above the horizon (and the angle of the sun above the horizon) continues to decrease as the period progresses.

2.2 Geomagnetic Field

The earth’s magnetic field produces a relative east-west shift in the apparent arrival direction of cosmic ray primaries from the direction of the moon. Older experiments ([13,14,15]) used the “impulse approximation” to calculate the expected 10 TeV proton deflection, 0.15° . Since the path a particle travels is fairly long, the “impulse approximation” may not be valid over such large distances. The geomagnetic deflection $\Delta\alpha$ of a given cosmic ray with charge Z and momentum p (TeV/c), depends strongly on the local magnetic field conditions, \vec{B} and the particle path \vec{l} . It can be written:

$$\tan(\Delta\alpha) = \frac{Z}{p} \int_0^{d_m} \vec{B} \times d\vec{l}, \quad (1)$$

where $d_m = 384 \times 10^3$ km is the distance from the earth to the moon. To measure the effect of geomagnetic deflection on the moon shadow the magnetic field encountered by a cosmic ray pri-

mary between the moon and the earth was integrated along the cosmic ray path. The integral was calculated numerically, with the cross product computed at 20 km intervals. Muons with arrival directions within a 2° half-angle cone of the moon's location were chosen from the data set. The geomagnetic field from the surface of the earth to 600 km was found using the International Geomagnetic Reference Field (IGRF) calculation [25]. The geomagnetic field from 600 km to the magnetopause (which varies depending on the IMF, here taken to be 70,000 km) was found using GEOPACK [26,27]. The geomagnetic field from the magnetopause to the location of the moon (384,000 km) was held constant at the value at 70,000 km. The muons that survive to the depth of the far detector are usually the decay products of mesons created in the first cosmic ray interaction, typically at a height of 20 km. The integrals were thus calculated using μ^+ with momentum $p_\mu = 0.1p_p$ from 0-20 km and protons from 20-384,000 km. The result of this calculation can be seen in Fig. 1, where the surface energy of each muon was set to 0.7 TeV, the vertical muon threshold energy of the far detector, and that $p_p = 10p_\mu$. The maximum deflection was $\Delta RA = 0.02^\circ$,

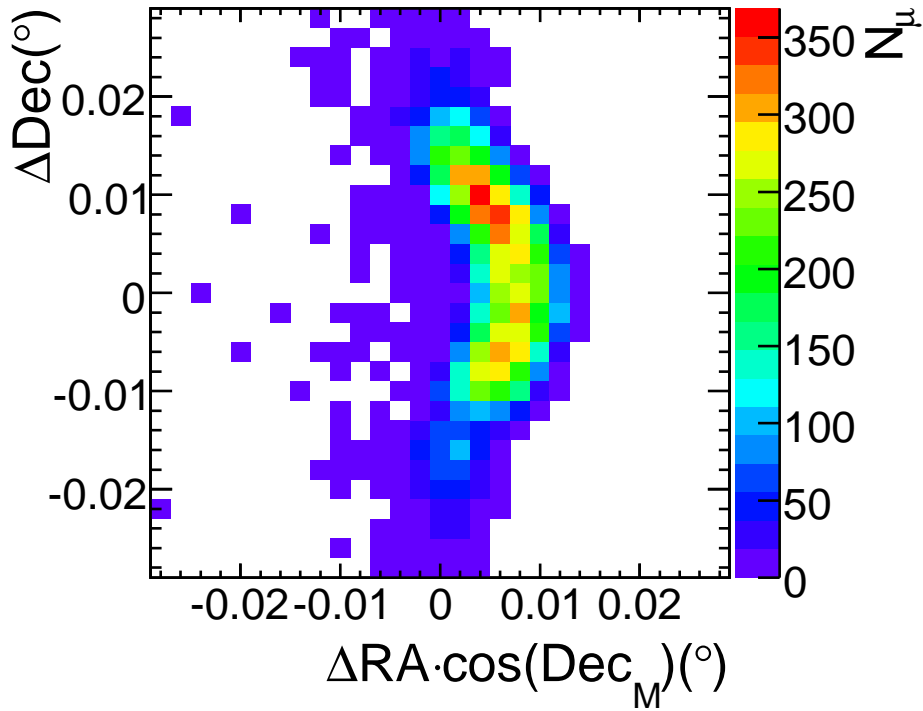


Fig. 1. The distribution of integrated geomagnetic deflections for cosmic rays that pass near the moon in horizon coordinates. This distribution is for the case where the muon energy was determined from the far detector overburden profile and each primary cosmic proton had energy $10p_\mu$.

and the mean deflection was $\Delta RA = 0.005^\circ$. Note that while there was a clear positive shift in RA , the distribution of deflections in Dec was more uniform. Any displacement of the moon shadow beyond 0.015° cannot be caused by the geomagnetic field, and it is unlikely that the geomagnetic field could cause an average deflection of greater than 0.01° .

2.3 Multiple Muons

In addition to the smearing effects of the geomagnetic and interplanetary magnetic fields, the cosmic muon angular resolution of an underground detector is limited by multiple Coulomb scattering in the surrounding rock as well as the geometric resolution of the apparatus itself. The geometric resolution of the detector is of order $\pm 0.15^\circ$ but the dominant effect 2070 mwe underground is multiple Coulomb scattering. The angular resolution of the detector was measured using 3.12 million multiple muon events with reconstructed multiplicity equal to two, collected from August 1, 2003 to December 31, 2007. Multiple muon events are created by a cosmic ray of sufficient energy to generate more than one energetic muon. The energy spectrum of multiple muon is similar to that of single muons, which is a steeply falling power law with a spectral index approximately minus three. Most muons (multiple muon events included) are close to the low energy cutoff. The transverse momentum of these pairs is negligible compared to their longitudinal momentum, and they have angular separation $< 0.05^\circ$ [14] at creation. The measured angular separation between these pairs quantifies the resolution of the detector. Pairs were selected by the same criteria used for single muons (see Sec. 2.1). A total of 1.77 million multiple muon events survived. The distribution of their angular separation ψ , divided by $\sqrt{2}$ to apply to the single muon resolution, is shown in Fig. 2. The resolution is defined to be the single muon angular separation within which

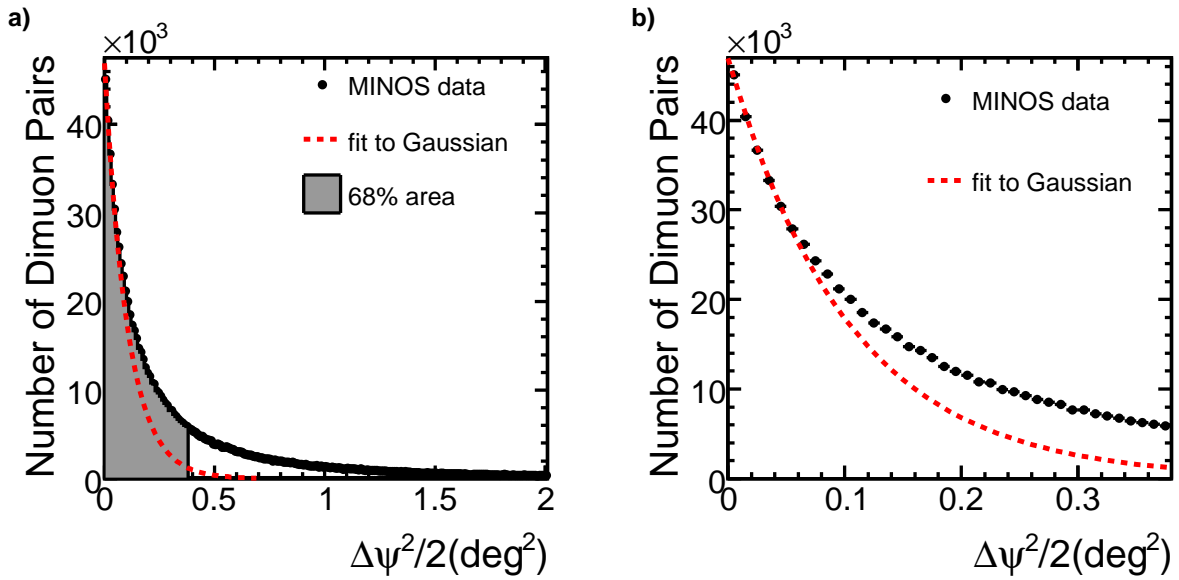


Fig. 2. a) The square of the single muon angular separation of multiple muon pairs, ψ , in deg^2 . The shaded region represents 68% of the distribution, which is taken to be the resolution of the detector, $\psi/\sqrt{2} = 0.62^\circ$. The peak region of the distribution was fitted with a Gaussian function, shown by the dashed line. The fit parameter $\sigma = 0.322 \pm 0.002^\circ$. b) The square of the single muon angular separation of multiple muon pairs out to 0.375 deg^2 .

68% of the distribution lies. This value, shown by the shaded region in Fig. 2, is 0.62° . The peak region of the distribution was fitted with a Gaussian function, shown by the dashed line. The fit parameter $\sigma = 0.322 \pm 0.002$. The Gaussian function fits well over the first few bins, which describes the bulk of the distribution, but the long tail begins to deviate from the Gaussian function at

$\psi^2/2 \sim 0.06 \text{ deg}^2$. The long tail can be attributed to Moliere scattering in the rock overburden [13].

2.4 Monte Carlo Simulation

The backgrounds for the shadow analyses were calculated using a *Monte Carlo* simulation. A muon arrival direction was chosen out of the known distribution of events in the detector (in horizon coordinates) and paired with a random time chosen from the known time distribution to find the muon's location in celestial coordinates. This was done for every data muon to create one background sample, and 1,000 background samples were created.

A template of the expected distribution of the sun and moon shadows in celestial coordinates (right ascension (RA) and declination (Dec)) was simulated using the detector resolution determined from the multiple muon events in Sec. 2.3 to account for the smearing effects of coulomb scattering and detector resolution. Cosmic rays were generated traveling towards a disk the size of the moon or sun. If the cosmic ray intercepted the disk it was removed. If not, the cosmic ray was assumed to produce a muon that would travel underground to the detector, and an angular deviation was selected at random from the multiple muon distribution. The resulting distribution in $\Delta RA \cdot \cos(Dec)$ ($\cos(Dec)$ normalizes for solid angle) and ΔDec can be seen for the moon in Fig. 3.

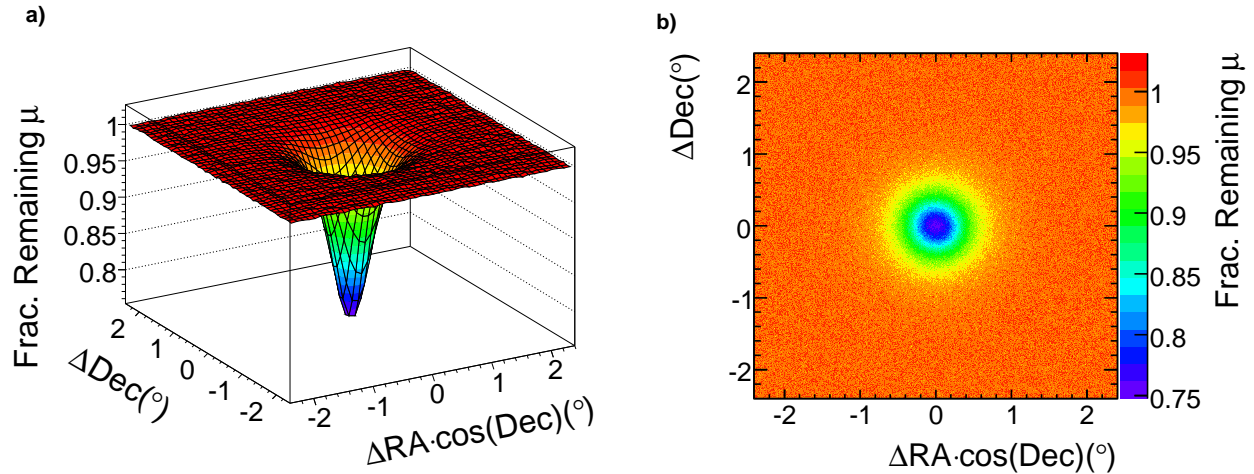


Fig. 3. The expected cosmic ray shadow of the moon (from simulation) as seen in the far detector, in two different views: a) in three dimensions, and b) in a two dimensional projection of a). It is shown in celestial coordinates centered on the location of the moon. The color axis shows the surviving fraction of cosmic-ray induced muons.

3 Moon Shadow

3.1 Two Dimensional Shadow

A two dimensional maximum likelihood grid search was used to find the location of the moon. The muons in the background samples generated in Sec. 2.4 were sorted by separation from the moon's location in equal solid angle bins 0.01° on a side. The x coordinate is given by $\Delta RA = (RA_\mu - RA_M) \cdot \cos(Dec_M)$, where the subscripts μ and M denote muon and moon, respectively, and the y coordinate is given by $\Delta Dec = (Dec_\mu - Dec_M)$. ΔRA is modified by $\cos(Dec_M)$ to account for the projection of sphere onto a flat grid. One thousand cosmic ray background samples were averaged to create a smooth, isotropic background grid. The data were sorted in a similar grid. A grid search utilizing a log-likelihood method was employed to find the most probable position of a moon-like deficit. This method was invented by Cash [28], first applied by COS-B [29], and first applied to the moon shadow by MACRO [14]. The moon shadow template (Sec. 2.4) was placed at a fixed position (x_s, y_s) on the data grid. The search was then performed by integrating over the the shadow template at this location. The template was then moved to adjacent bin location (x_s, y_{s+1}) , and the search was repeated. This process was repeated until the entire 4° by 4° data grid was scanned. The shadow that fit the data best was found by maximizing the shadow strength I_s using the likelihood function:

$$l(x, y, I_s) = 2 \sum_{i=1}^{n_{bin}} \left[N_i^{th} - N_i^{obs} + N_i^{obs} \ln \frac{N_i^{obs}}{N_i^{th}} \right], \quad (2)$$

where $N_i^{th} = N_i^{back} - I_s \cdot P_s(x_i, y_i)$ is the number of events expected in bin i , N_i^{back} is the number of muons from the smoothed background grid in bin i and $P_s(x_i, y_i)$ is the fraction of the cosmic rays at location (x_i, y_i) blocked by the moon, and is equal to one minus the distribution in Fig 3. $I_s \cdot P_s(x_i, y_i)$ is the number of events removed from bin i by the moon. To determine the strength of this deficit, the parameter Λ was defined as:

$$\Lambda = l(x, y, 0) - l(x, y, I_s), \quad (3)$$

which is a measure of the deviation from the null (no-moon) hypothesis.

The two dimensional distribution of these deviations was drawn on a $4^\circ \times 4^\circ$ grid, binned in 0.01° on a side, and can be seen in Fig. 4 in celestial coordinates. The greatest deficit is $\Lambda = 30.9$, centered on $(-0.11 \pm 0.09^\circ, -0.13 \pm 0.08^\circ)$. This is consistent with the Soudan 2 [13] shadow, which was offset by 0.1° E-W and 0.1° N-S. The error and maximal value was found by drawing a 1σ contour around the bin location of Λ_{max} . The value of I_s at this location was 0.13, in which 235.2 events were removed by the moon, which is consistent with the expectation of 297.8 events removed. In the high statistics limit, the distribution of Λ is the same as for a χ_ν^2 distribution [28], where ν is the number of free parameters. In this case there is only one free parameter, I_s , which means $\Lambda = 30.9$ has a significance of 5.6σ .

A second method was used as a cross-check to find the significance of the observed deficit. Moon-

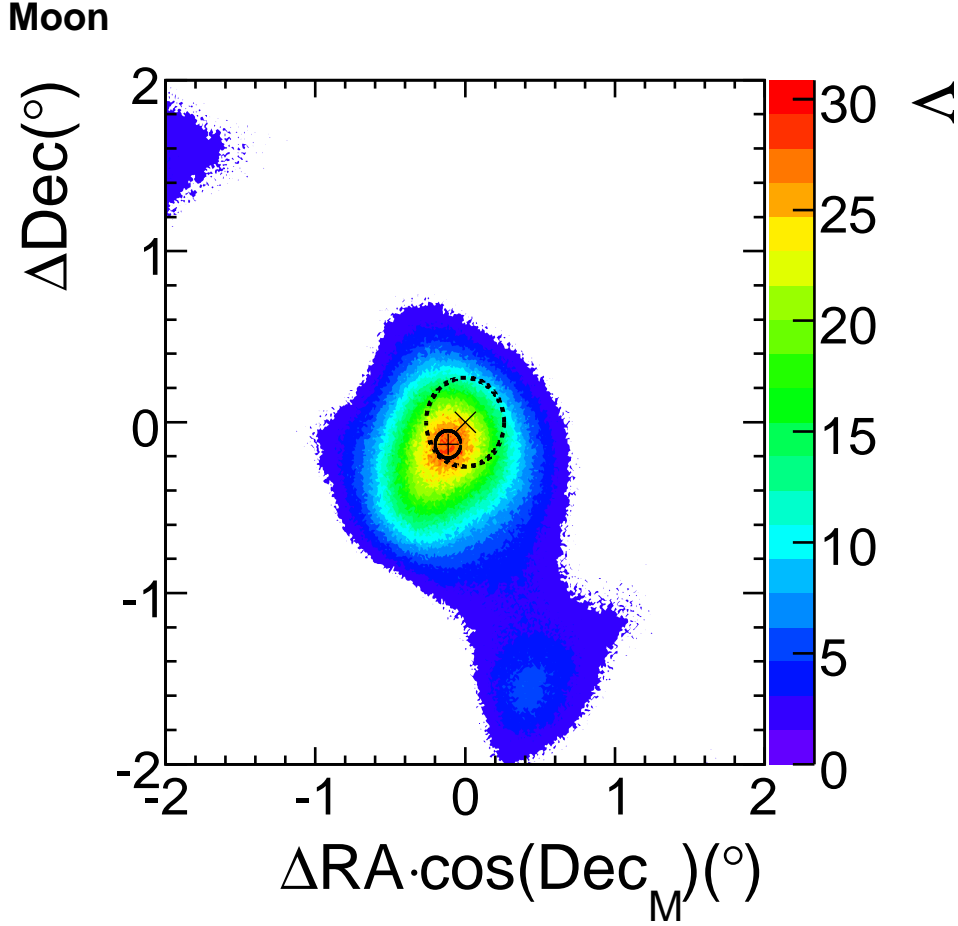


Fig. 4. The two dimensional moon induced muon deficit in 0.01° wide bins, in celestial coordinates. The \times marks the expected location of the moon, and the dashed circle is the apparent size of the moon as viewed from earth. The cross marks the observed location of the moon, and the solid ellipse denotes the uncertainty. The greatest deficit is $\Lambda = 30.9$, a 5.6σ significance, centered on $(-0.11^\circ, -0.13^\circ)$

less grids were created using the same background method described in Sec. 2.4. Searching through many moonless grids gave the probability of randomly finding a moon-like deficit for a particular value of Λ . Each $4^\circ \times 4^\circ$ grid allowed 160,000 searches, for a total of 161.4 million searches. There were no searches that had $\Lambda > 23.0$ and the distribution of Λ followed the expected χ_1^2 distribution.

3.2 One Dimensional Shadow

As a check on the resolution of the detector, a one dimensional moon shadow search was performed. The differential density of cosmic rays obscured by the moon, $\Delta N_\mu / \Delta \Omega$, can be written as a two dimensional Gaussian convolution in polar coordinates (r, ϕ) :

$$\frac{\Delta N_\mu}{\Delta \Omega} = \lambda \left(1 - \frac{1}{2\pi\sigma^2} \int_0^{R_m} r' dr' \int_0^{2\pi} d\phi e^{-(r^2+r'^2-2rr' \cos \phi)/2\sigma^2} \right) \quad (4)$$

where λ is the average differential muon flux, σ accounts for smearing from detector resolution, multiple Coulomb scattering and geomagnetic deflection, and $R_m = 0.26^\circ$, the radius of the moon or sun. Performing the integration over ϕ gives:

$$\frac{\Delta N_\mu}{\Delta\Omega} = \lambda \left(1 - \frac{1}{\sigma^2} \int_0^{R_m} r' dr' I_0 \left(\frac{rr'}{\sigma^2} \right) e^{-\frac{r^2}{2\sigma^2}} \right), \quad (5)$$

where I_0 is a modified Bessel function of the first kind. The integral that remains has no closed-form solution; however I_0 has a rapidly decreasing Taylor expansion:

$$I_0(x) = \sum_{k=0}^{\infty} \frac{2^{2k}}{4^k (k!)^2} = 1 + \frac{x^2}{4} + \frac{x^4}{64} + \frac{x^6}{2304} + \dots \quad (6)$$

Substituting the expansion and evaluating the integral gives:

$$\frac{\Delta N_\mu}{\Delta\Omega} = \lambda \left[1 - \frac{R_m^2}{2\sigma^2} e^{-\theta^2/2\sigma^2} \left(1 + \frac{(\theta^2 - 2\sigma^2)R_M^2}{8\sigma^4} + \frac{(\theta^4 - 8\theta^2\sigma^2 + 8\sigma^4)R_M^4}{192\sigma^8} \right) \right], \quad (7)$$

with $\theta = r$ since the observable in this case is an angular separation. This formula automatically produces a deficit of $\pi R_m^2 \lambda$ events due to shadowing. The significance of the deficit can be found by fitting to Eq. 7 and finding the difference between this χ^2 value and the χ^2 value obtained by a linear fit to the same data.

3.3 Search in One Dimension

The reconstructed muon angular separation from the moon or sun, $\Delta\theta$, was binned in $S_{\text{bin}} = 0.10^\circ$ increments. Since radial distance from the center is measured over a two dimensional projection, the solid angle of bin (i) increases when moving out from the center as $\Delta\Omega_i = (2i - 1) \cdot S_{\text{bin}}^2 \pi$. Weighting the number of events in each bin by the reciprocal of the area resulted in the distribution $N_i/\Delta\Omega_i$, the differential muon density.

Since the location of the moon was found to be offset from $(0^\circ, 0^\circ)$, the arrival direction of each muon was adjusted by $(0.11^\circ, 0.13^\circ)$ before performing the one dimensional moon shadow search. The position of the moon on the sky and the separation of each muon from the moon ($\Delta\theta$), was found using the method described in Sec. 2.1. The $\Delta\theta$ distribution is shown in Fig. 5 with statistical error bars. There is a significant deficit in the location of the moon as $\Delta\theta \rightarrow 0$ attributed to the moon's blocking of the primary cosmic rays. A linear (no moon deficit) fit gives a $\chi_L^2/ndf = 57.8/39$. A fit to Eq. 7 (moon induced deficit) gives a $\chi_G^2/ndf = 25.3/38$. The improvement in χ^2 of 32.6 corresponds to a significance of 5.6σ . The resolution found by this method is $\sigma = 0.34 \pm 0.04^\circ$, which is consistent with a Gaussian fit to the multiple muon data shown in Fig. 2. When the same analysis is performed without shifting the muons by $(0.11^\circ, 0.13^\circ)$, the significance of the moon shadow is reduced by 2.7σ , and the shadow is more smeared out, with $\sigma = 0.39 \pm 0.06^\circ$.

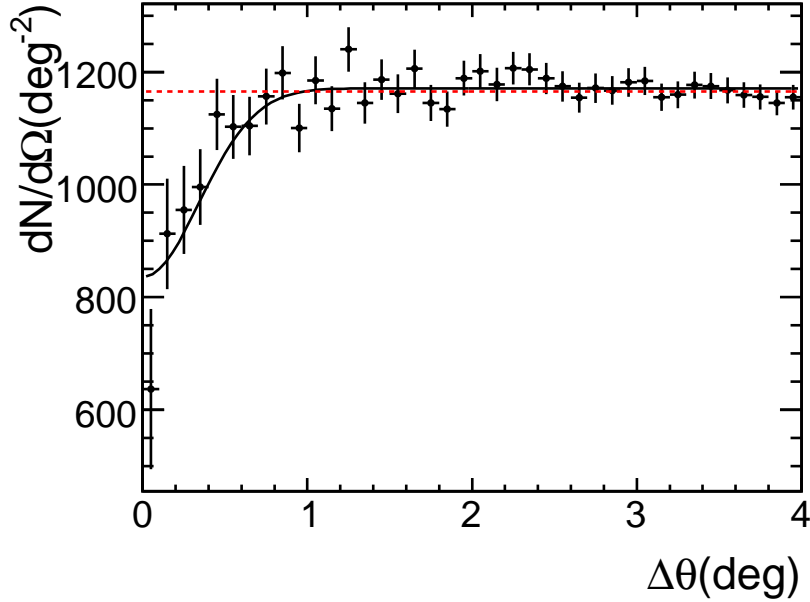


Fig. 5. The differential muon flux with respect to displacement from the moon’s location, binned in $\Delta\theta = 0.1^\circ$. The dashed curve is the result of a linear (no moon effect) fit, which gives $\chi_L^2/ndf = 57.8/39$. The solid curve is the best fit from Eq. 7. The Gaussian (moon-induced deficit) fit gives $\chi_G^2/ndf = 25.3/38$, with parameters $\lambda = 1171.1 \pm 4.8$ and $\sigma = 0.34 \pm 0.04^\circ$.

4 Sun Shadow

As viewed from earth, the sun also obscures a 0.52° diameter disk, approximately the same size as the moon. The one dimensional shadowing procedure from Sec. 3 and the two dimensional log-likelihood analysis described in Sec. 3.1 were performed for cosmic ray muons coming from the direction of the sun. Historically, this has been a more difficult [15] measurement to make because of the variability of the sun’s magnetic field described in Sec. 5.

The two dimensional sun shadow can be seen in Fig. 6. The sun $\Lambda_{max} = 14.6$ occurs at $(-0.29 \pm 0.13^\circ, 0.27 \pm 0.14^\circ)$ and has a 3.8σ significance. The value of I_s at this location was 0.08, in which 144.6 events were removed by the sun, which is about half of the expected of 279.8 events removed. The sun shadow has a Λ_{max} value that is less than half the Λ_{max} value of the moon, and the shadow appears elongated along a line through the origin, rotated about halfway between the north and to the west. These features could be attributed to a smearing effect that is unobserved in the moon shadow, originating from the longer exposure to the IMF along the much greater path between the sun and the earth.

The one dimensional sun shadow can be seen in Fig. 7. Note that the muons were shifted by $(0.29^\circ, -0.27^\circ)$ to account for the offset from the expected location of the sun given by the two dimensional sun shadow. There is a significant deficit in the location of the sun attributed to the sun’s blocking of the primary cosmic rays. The improvement in χ^2 of 15.1 ($\chi_L^2/ndf = 67.9/39$, $\chi_G^2/ndf = 52.8/38$) corresponds to a 3.9σ significance. The Gaussian fit parameter $\sigma = 0.48 \pm 0.07$ for the

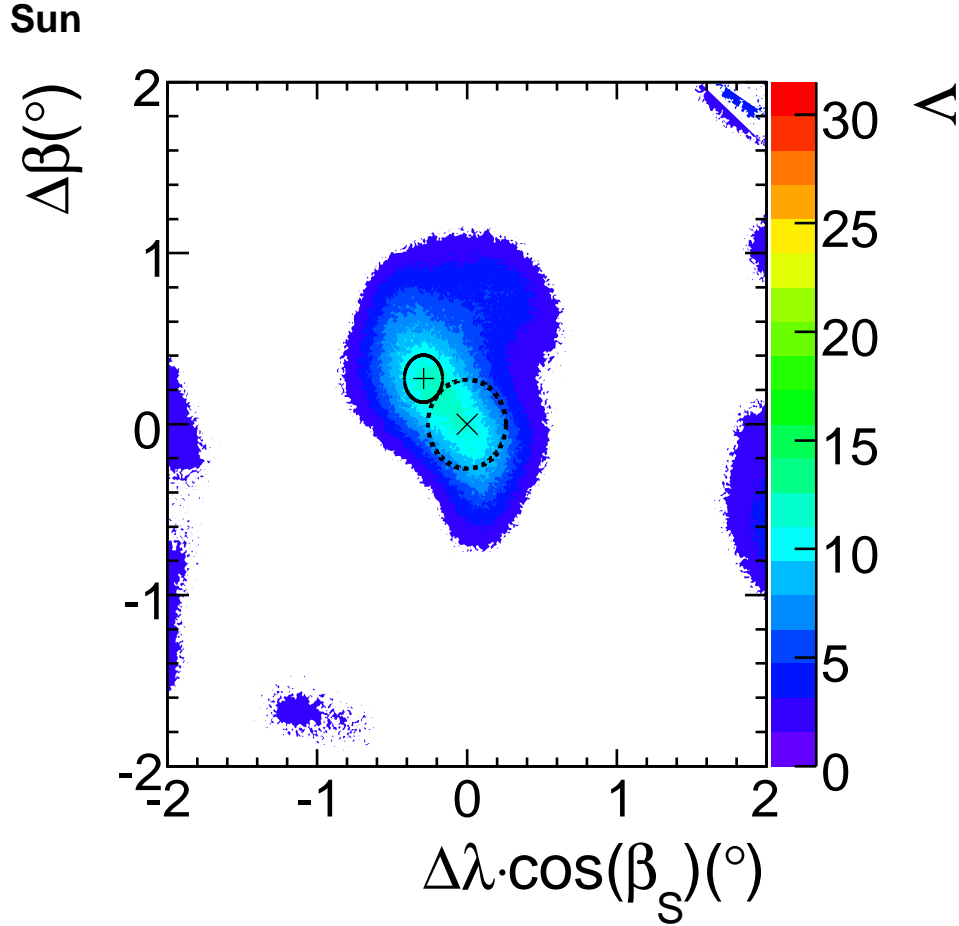


Fig. 6. The two dimensional sun induced muon deficit in 0.01 deg^2 bins, in ecliptic coordinates. The \times marks the expected location of the sun, and the dashed circle is the apparent size of the sun as viewed from earth. The cross marks the observed location of the sun, and the solid ellipse denotes the uncertainty. The greatest deficit is $\Lambda_{max} = 14.6$, a 3.8σ significance, centered on $(-0.29^\circ, 0.27^\circ)$. The maximum of the color scale is set to $\Lambda = 31$ to allow for easy comparison with the moon shadow.

sun shadow is somewhat larger than the value found by the fit to the moon shadow, $\sigma = 0.34 \pm 0.04$.

5 Interplanetary Magnetic Field Effects

5.1 Moon Shadow

The IMF could have some effect on the moon shadow by the effects described in Sec. 1. This could be observed by dividing the data into separate day/night samples as cosmic rays experience the maximal IMF difference when approaching the earth from the day and night sides. The effect of the IMF on the geomagnetic field is to produce a reduced geomagnetic field at night [26,27,30]. This effect was observed by MACRO [15]. Daytime is defined here as when the sun's zenith angle

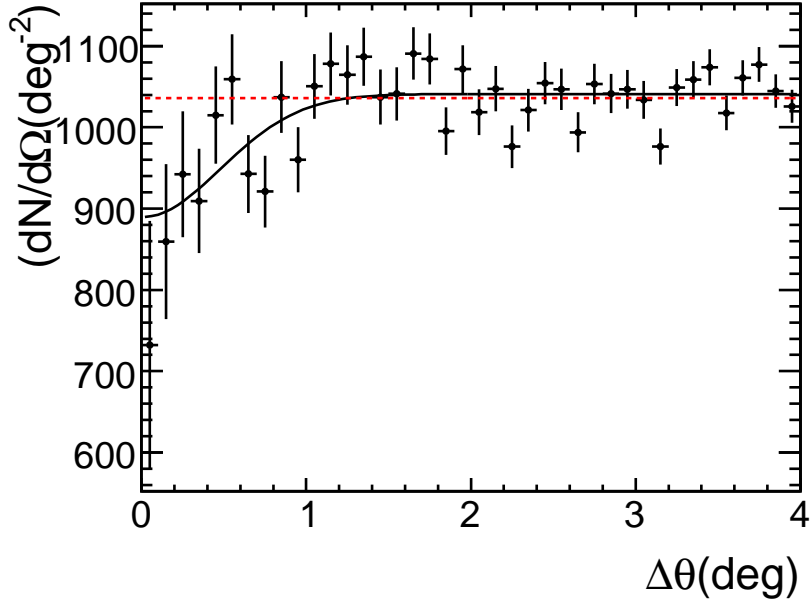


Fig. 7. The differential muon flux with respect to displacement from the sun’s location, binned in 0.10° . A linear (no sun effect) fit gives $\chi_L^2/ndf = 67.9/39$. The solid curve is the best fit from Eq. 7. The Gaussian (sun-induced deficit) fit gives $\chi_G^2/ndf = 52.8/38$, with parameters $\lambda = 1040.9 \pm 4.6$ and $\sigma = 0.48 \pm 0.073^\circ$.

was less than zero. The day-time sample contained 8,270 muons within a 2° half-angle cone around the moon, while the night-time sample contained 9,213 events. The reason for this difference is that the detector is only down for maintenance during the day, coupled with the fact that more of the data were collected in the fall and winter than spring and summer (see Sec. 2.1). Integrating over five and a half years accounts for the 10% increase in muons collected near the moon at night. The moon shadow observed at night can be seen in Fig. 8 (Left), while the moon shadow during the day can be seen in Fig. 8 (Right). The center of the deficit is at $(-0.09 \pm 0.11^\circ, -0.22 \pm 0.13^\circ)$ with $\Lambda_{max}^{night} = 23.7 (4.9 \sigma)$ for the data taken at night. For the data taken during the day, the center of the deficit is at $(-0.21 \pm 0.12^\circ, -0.07 \pm 0.12^\circ)$, with $\Lambda_{max}^{day} = 11.2 (3.3 \sigma)$. Λ_{max}^{night} is consistent with the expected location of the moon in ΔRA , while the shadow during the day is shifted by 1.7σ . The shift in ΔRA at night is consistent with zero. The shift in ΔDec at night, however, is further from the expected location of the moon by 1.7σ . It is unlikely that the geomagnetic field could cause a deflection of greater than -0.02° (Sec. 2.2) and the geomagnetic field should not cause a diurnal effect. A possible explanation is that the IMF has a general defocussing effect on cosmic rays, and cosmic rays detected at night experience less of this IMF effect because they arrive at earth from the opposite direction to the sun.

5.2 Sun Shadow

A greater IMF means a less prominent sun shadow, so the significance of the observable shadowing caused by the sun should decrease as the IMF increases. Since the IMF is caused by solar activity,

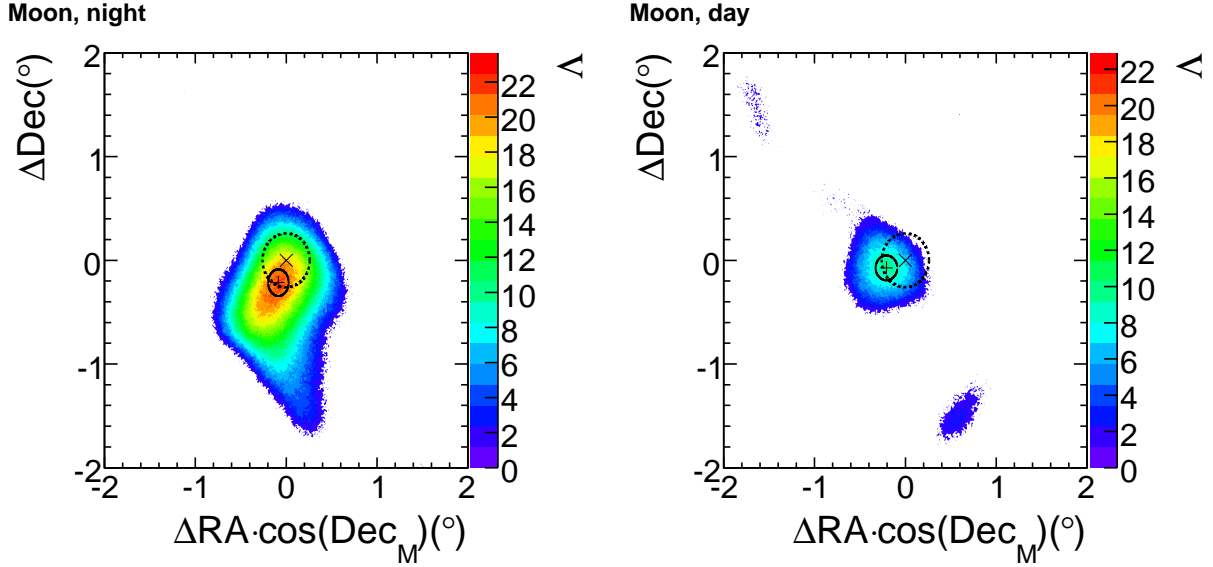


Fig. 8. The distribution of Λ values in celestial coordinates when the moon was visible during the night (Left), and when the moon was visible during the day (Right). The \times marks the expected location of the moon, and the dashed circle is the apparent size of the moon as viewed from earth. The cross marks the observed location of the moon, and the solid ellipse denotes the uncertainty. The deficit has $\Lambda_{max}=23.7$ (4.9σ) at night, and the center is at $(-0.09 \pm 0.11^\circ, -0.22 \pm 0.13^\circ)$. The deficit has $\Lambda_{max}=11.2$ (3.3σ) in the day, and the center is at $(-0.21 \pm 0.12^\circ, -0.07 \pm 0.12^\circ)$.

the significance of observable shadowing should increase as the number of sunspots, one measure of solar activity, decreases. The last maximum of the 11 year solar cycle occurred in 2001, and the next minimum occurred in December, 2008 [23]. To search for a correlation between solar activity and strength of sun shadowing effects, the data were divided into five separate one dimensional grids of roughly equal statistics, and fit with both a linear function and a one-parameter Gaussian (Eq. 7), holding the number of removed muons constant. The one dimensional search is used because it requires fewer events to produce a statistically significant shadow and the sun was shown to be close to the center of the grid (see Fig. 6). There were not enough accumulated muons to perform five of the two dimensional likelihood searches. The periods were Aug. 1, 2003 - Sep. 30, 2004, Oct. 1, 2004 - Oct. 31, 2005, Nov. 1, 2005 - Nov. 30, 2006, Dec. 1, 2006 - Dec. 31, 2007 and Jan. 1, 2008 - Dec. 31, 2008. These graphs can be seen in Fig. 9.

The results of these fits are summarized in Table 2. There is a decrease in the size (σ) and corresponding error of the sun shadow as the sun approaches solar minimum. This decline could be correlated to the decrease in solar activity. Surprisingly, the period nearest to solar minimum, January 1, 2008-December 31, 2008, shows an increased size. For comparison, the yearly moon shadows for the same periods were calculated and summarized in Table 2. The moon shadow has more constant size over the five periods than does the sun.

A more useful correlation between the sun shadow and the IMF is to perform two dimensional searches on data sets subdivided according to the vector components of the IMF, but there are problems with this approach. First of all, the number of data subsets is limited to two, because the 2D log-likelihood analysis is statistically limited. Second, the IMF is known to have a complicated and time-varying structure. The ACE, Wind and IMP 8 spacecraft, which monitor the IMF while

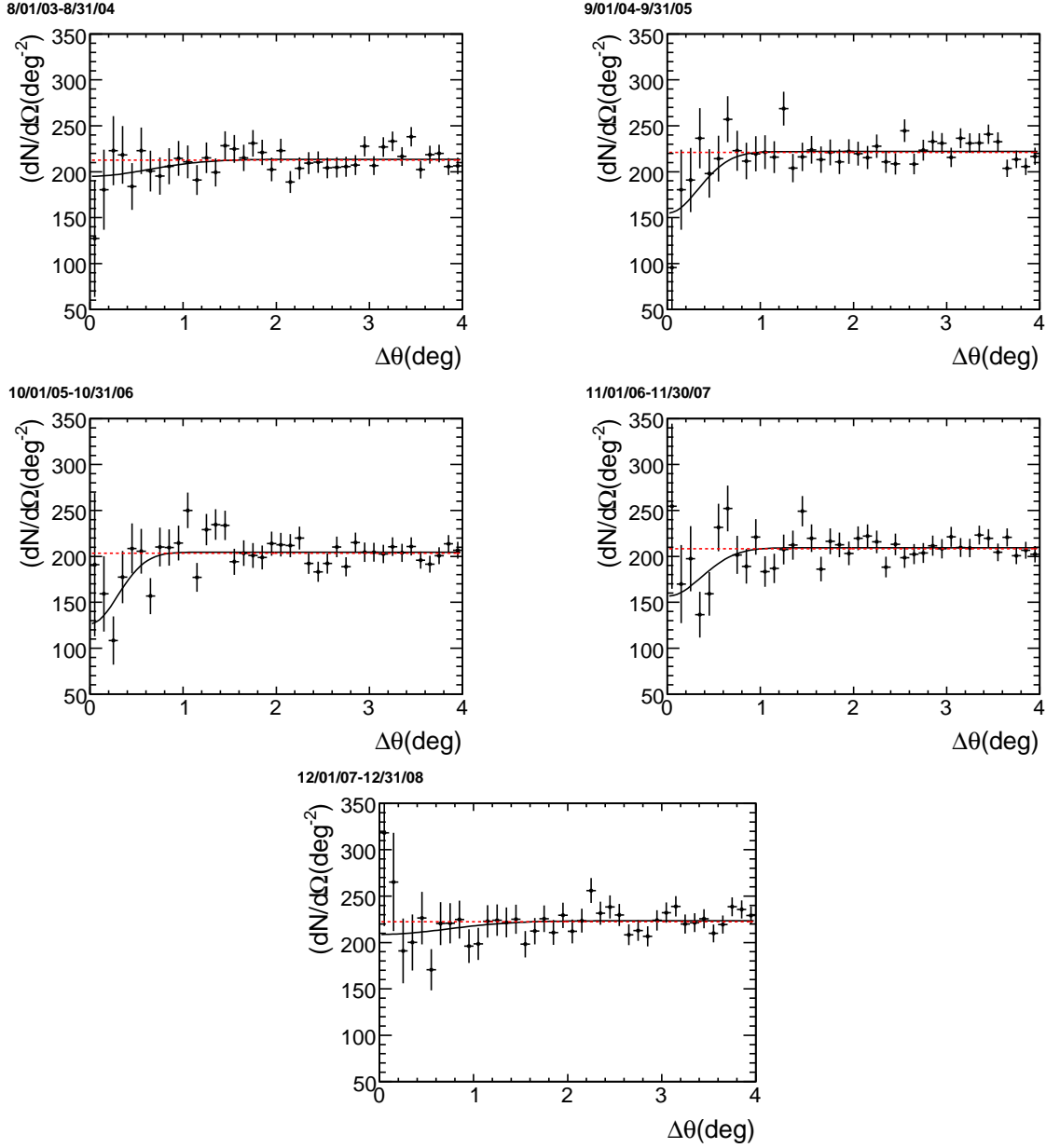


Fig. 9. The differential muon flux with respect to displacement from the sun’s location as a function of year, binned in 0.1° . The dashed curve is a linear (no sun effect) fit, while the solid curve is the best fit from Eq. 7.

orbiting about the L1 Lagrange point (225 earth radii in front of earth), report data averaged over one hour [31]. These data report the IMF in Geocentric Solar Ecliptic (GSE) coordinates, where the earth-sun line defines the x-axis, and the ecliptic north pole is the z-axis. It is difficult to adequately account for the variations in the field with these data, as was done in Sec. 2.2 for the geomagnetic field. The greatest difficulty is the fact that the IMF data is only available every hour for one location in space, whilst it is well known that the IMF changes somewhat rapidly in time and has a sectorized structure [21]. The direction of the IMF is either “toward” or “away” from the earth, and the two field directions are separated by a thin layer known as the neutral current sheet, which passes the L1 point very briefly as the x component of IMF reverses polarity.

Table 2

The size of shadowing observed in each year’s sun distribution. Also included is the corresponding moon shadow size. The significance is given in units of standard deviations (s.d.).

	Sun			Moon		
Distribution	σ	χ_G^2	Significance	σ	χ_G^2	Significance
Aug. 1, 2003 - Sep. 30, 2004	0.61 ± 0.28	34	1.6 s.d.	0.34 ± 0.11	27.4	1.9 s.d.
Oct. 1, 2004 - Oct. 31, 2005	0.31 ± 0.12	42.3	1.6 s.d.	0.33 ± 0.08	24	4.0 s.d.
Nov. 1, 2005 - Nov. 30, 2006	0.27 ± 0.07	45.5	3.2 s.d.	0.19 ± 0.04	38.6	3.9 s.d.
Dec. 1, 2006 - Dec. 31, 2007	0.34 ± 0.12	42.3	2.5 s.d.	0.33 ± 0.11	32.2	3.6 s.d.
Jan. 1, 2008 - Dec. 31, 2008	0.70 ± 0.29	37.2	2.1 s.d.	0.26 ± 0.06	42.6	3.4 s.d.

These IMF data were used to separate the muon data and search for IMF induced effects. The data were first separated into two sets by the magnitude in the expected deflection plane, which is perpendicular to the earth-sun line. The “large magnitude” set was where $|B_{\perp}| > 4.2$ nT; less than 4.2 nT was the “small magnitude” data set. No significant translation of the shadow nor focusing effects were observed. The shadows had magnitudes equal to roughly half of the total sun shadow, consistent with what was expected from dividing the data set in half arbitrarily.

An interesting effect was observed when the data were divided into sets where the IMF component along the earth-sun line (B_x) was greater and less than zero. For the $B_x > 0$ case, the most significant deficit was centered on $(-0.07 \pm 0.14^\circ, 0.10 \pm 0.12^\circ)$, which is consistent with the expected location of the sun. This shadow shows none of the elongation seen in the total sun shadow (Fig. 6). For the $B_x < 0$ case, the most significant deficit was centered on $(-0.41 \pm 0.17^\circ, 0.47 \pm 0.20^\circ)$. In fact, this shadow has almost no significance near the expected location of the sun, and has two deficits of almost equal significance an equal distance from the center. This offset is 2.4σ in RA and 2.3σ in Dec from the location of the sun. The sectorized structure of the IMF causes a cosmic ray traveling along the path from the sun to the earth to experience magnetic deflections in a multitude of directions. The rotating nature of the IMF adds an additional element to the magnetic deflection. It may be that the “inward” and “outward” separation of the cosmic ray data set along the earth-sun line is a more consistent predictor of cosmic ray deflection than the sparse measurements of the IMF in the y and z directions.

6 Conclusions

Using 52.3 million muons accumulated over 1857.91 live-days, the MINOS far detector has observed the cosmic ray shadow of both the moon and sun with high significance. The two dimensional moon shadow was seen with a significance of 5.6σ , centered on $(-0.11 \pm 0.09^\circ, -0.13 \pm 0.08^\circ)$, which suggests that the absolute pointing of the detector on the sky is known to $0.17 \pm 0.12^\circ$. The significance of the one dimensional moon shadow increased after shifting the muon arrival directions by $(-0.11^\circ, -0.13^\circ)$ to be consistent with the observed location of the moon. The cosmic

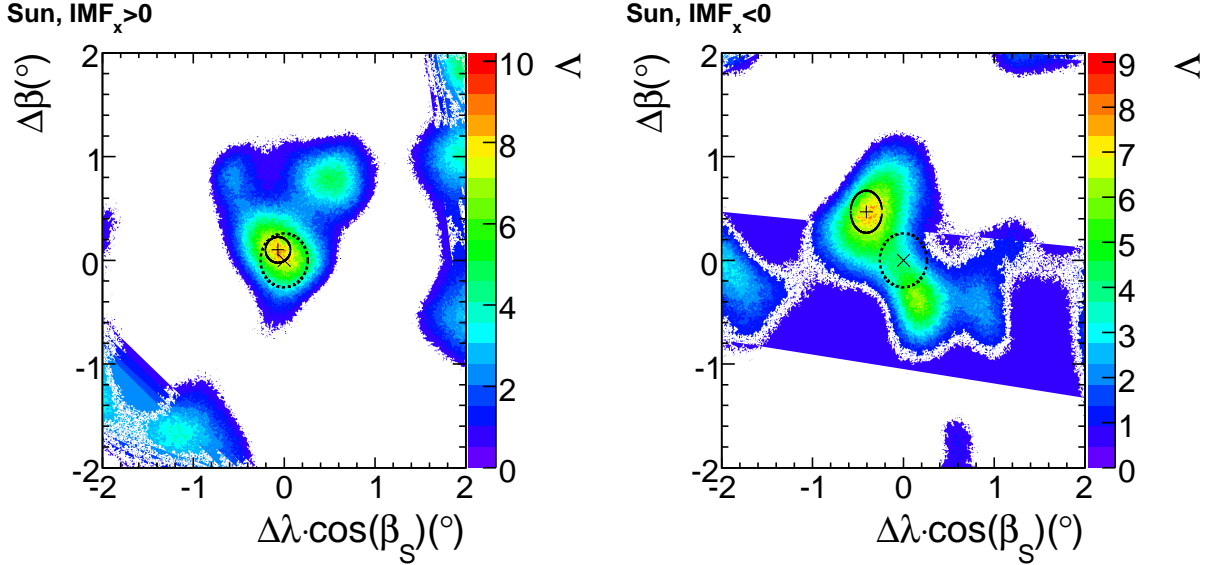


Fig. 10. The sun shadow for $B_x > 0$ (Left) and $B_x < 0$ (Right). The \times marks the expected location of the sun, and the dashed circle is the apparent size of the sun as viewed from earth. The cross marks the observed location of the sun, and the solid ellipse denotes the uncertainty. The most significant deficit was located at $(-0.07 \pm 0.14^\circ, 0.10 \pm 0.12^\circ)$ and had $\Lambda_{max} = 10.2$ (3.2σ) for $B_x > 0$. The most significant deficit was located at $(-0.41 \pm 0.17^\circ, 0.47 \pm 0.20^\circ)$ and had $\Lambda_{max} = 9.2$ (3.0σ) for $B_x < 0$.

ray shadow of the sun over the same time period was measured in two dimensions with a significance 3.8σ , centered on $(-0.29 \pm 0.13^\circ, 0.27 \pm 0.14^\circ)$.

Searches were made for possible dependencies of the moon and sun shadow on the IMF but no three sigma effects were observed. At lesser statistical significance, effects were observed in the difference of the moon shadow during the day and night and in the variation of the sun shadow with time. The shadow of the sun showed some indication (though less than three sigma) of variation with the x component of the IMF, which could be interpreted as focusing (for $B_x > 0$) and defocussing (for $B_x < 0$). These latter observations of short term correlations with the IMF were made at the limit of the experiment's statistical power, and it will be interesting for other detectors to confirm these signals.

7 Acknowledgments

We thank the Fermilab staff and the technical staffs of the participating institutions for their vital contributions. This work was supported by the U.S. Department of Energy, the U.S. National Science Foundation, the U.K. Science and Technologies Facilities Council, the State and University of Minnesota, the Office of Special Accounts for Research Grants of the University of Athens, Greece, FAPESP (Fundação de Amparo à Pesquisa do Estado de São Paulo), CNPq (Conselho Nacional de Desenvolvimento Científico e Tecnológico) in Brazil. We gratefully acknowledge the Minnesota Department of Natural Resources for their assistance and for allowing us access to the facilities of the Soudan Underground Mine State Park and the crew of the Soudan Underground

Physics laboratory for their tireless work in building and operating the MINOS detector.

References

- [1] D. G. Michael, et al., The magnetized steel and scintillator calorimeters of the MINOS experiment, *Nucl. Instrum. Methods* 596 (2008) 190–228.
- [2] P. Adamson, et al., A Study of Muon Neutrino Disappearance Using the Fermilab Main Injector Neutrino Beam, *Phys. Rev. D* 77 (2008) 072002.
- [3] B. J. Rebel, Neutrino induced muons in the MINOS far detector, PhD Dissertation, Indiana University FERMILAB-THESIS-2004-33.
- [4] P. Adamson, et al., Observation of muon intensity variations by season with the MINOS far detector, Submitted to *Phys. Rev. D*, hep-ex/09094012.
- [5] M. Ambrosio, et al., Search for cosmic ray sources using muons detected by the MACRO experiment, *Astropart. Phys.* 18 (2003) 615–627.
- [6] G. W. Clark, Arrival Directions of Cosmic-Ray Air Showers from the Northern Sky, *Physical Review* 108 (1957) 450–457.
- [7] D. E. Alexandreas, et al., Observation of shadowing of ultrahigh-energy cosmic rays by the moon and the sun, *Phys. Rev. D* 43 (1991) 1735–1738.
- [8] A. Borione, et al., Observation of the shadows of the Moon and Sun using 100-TeV cosmic rays, *Phys. Rev. D* 49 (1994) 1171–1177.
- [9] M. Amenomori, et al., Cosmic ray deficit from the directions of the Moon and the Sun detected with the Tibet air shower array, *Phys. Rev. D* 47 (1993) 2675–2681.
- [10] R. W. Atkins, et al., Milagrito, a TeV air-shower array, *Nucl. Instrum. Meth.* A449 (2000) 478–499.
- [11] A. Oshima, S. R. Dugad, U. D. Goswami, S. K. Gupta, Y. Hayashi, N. Ito, A. Iyer, P. Jagadeesan, A. Jain, S. Kawakami, M. Minamino, P. K. Mohanty, S. D. Morris, P. K. Nayak, T. Nonaka, S. Ogio, B. S. Rao, K. C. Ravindran, H. Tanaka, S. C. Tonwar, GRAPES-3 Collaboration, The angular resolution of the GRAPES-3 array from the shadows of the Moon and the Sun, *Astroparticle Physics* 33 (2010) 97–107.
- [12] M. Merck, A. Karle, S. Martinez, F. Arqueros, K. H. Becker, M. Bott-Bodenhausen, R. Eckmann, E. Faleiro, J. Fernandez, P. Fernandez, V. Fonseca, V. Hausteiner, G. Heinzlmann, I. Holl, F. Just, F. Krennrich, M. Kühn, E. Lorenz, H. Meyer, N. Müller, R. Plaga, J. Prah, M. Probst, M. Rozanska, M. Samorski, H. Sander, K. Sauerland, C. Seseña, W. Stamm, Methods to determine the angular resolution of the HEGRA extended air shower scintillator array, *Astroparticle Physics* 5 (1996) 379–392.
- [13] J. H. Cobb, et al., The observation of a shadow of the moon in the underground muon flux in the Soudan 2 detector, *Phys. Rev. D* 61 (2000) 092002.
- [14] M. Ambrosio, et al., Observation of the shadowing of cosmic rays by the moon using a deep underground detector, *Phys. Rev. D* 59 (1998) 012003.

- [15] M. Ambrosio, et al., Moon and sun shadowing effect in the MACRO detector, *Astropart. Phys.* 20 (2003) 145–156.
- [16] P. Achard, et al., Measurement of the shadowing of high-energy cosmic rays by the moon: A search for tev-energy antiprotons, *Astropart. Phys.* 23 (2005) 411–434.
- [17] Y. M. Andreyev, V. N. Zakidyshev, S. N. Karpov, V. N. Khodov, Observation of the Moon Shadow in Cosmic Ray Muons, *Cosmic Research* 40 (2002) 559–564.
- [18] M. Urban, P. Fleury, R. Lestienne, F. Plouin, Can we detect antimatter from other galaxies by the use of the earth’s magnetic field and the moon as an absorber?, *Nucl. Phys. Proc. Suppl.* 14B (1990) 223–236.
- [19] J. Heintze, et al., Measuring the chemical composition of cosmic rays by utilizing the solar and geomagnetic fields In Adelaide 1990, *Proceedings, Cosmic ray*, vol. 4 456- 459.
- [20] E. N. Parker, Dynamics of interplanetary gas and magnetic fields, *Astrophys. J.* 128 (1958) 664.
- [21] J. M. Wilcox, N. F. Ness, Quasi-Stationary Corotating Structure in the Interplanetary Medium, *Journal of Geophysical Research* 70 (1965) 5793–5805.
- [22] M. Amenomori, et al., Direct evidence of the interplanetary magnetic field effect on the cosmic ray shadow by the sun, *Astrophys. J.* 415 (1993) L147–L150.
- [23] National Oceanographic and Atmospheric Administration, <http://www.swpc.noaa.gov/SolarCycle/>.
- [24] P. Adamson, et al., Measurement of the atmospheric muon charge ratio at TeV energies with MINOS, *Phys. Rev. D* 76 (2007) 052003.
- [25] I. A. of Geomagnetism & Aeronomy, International geomagnetic reference field IGRF-10.
- [26] N. A. Tsyganenko, Modeling the Earth’s magnetospheric magnetic field confined within a realistic magnetopause, *Journal of Geophysical Research* 100 (1995) 5599–5612.
- [27] N. A. Tsyganenko, D. P. Stern, Modeling the global magnetic field of the large-scale Birkeland current systems, *Journal of Geophysical Research* 101 (1996) 27187–27198.
- [28] W. Cash, Parameter estimation in astronomy through application of the likelihood ratio, *Astrophys. J.* 228 (1979) 939–947.
- [29] A. M. T. Pollock, et al., COS-B gamma-ray sources and interstellar gas in the first galactic quadrant - caravane collaboration for the COS-B satellite, *Astronomy and Astrophysics* 146 (1985) 352–362.
- [30] X.-W. Zhou, C. T. Russell, G. Le, N. Tsyganenko, Comparison of observed and model magnetic fields at high altitudes above the polar cap: POLAR initial results, *Geophysical Research Letters* 24 (1997) 1451–1454.
- [31] Goddard space flight center, omniweb, <http://omniweb.gsfc.nasa.gov/>.

